NANO LETTERS

Letter

pubs.acs.org/NanoLett

Independent Tuning of Electronic Properties and Induced Ferromagnetism in Topological Insulators with Heterostructure Approach

Zilong Jiang,[†] Cui-Zu Chang,[‡] Chi Tang,[†] Peng Wei,[‡] Jagadeesh S. Moodera,[‡,§] and Jing Shi*[,†]

[†]Department of Physics and Astronomy, University of California, Riverside, California 92521, United States

[‡]Francis Bitter Magnetic Lab and [§]Department of Physics, Massachusetts Institute of Technology, Cambridge, Massachusetts 02139, United States

Supporting Information

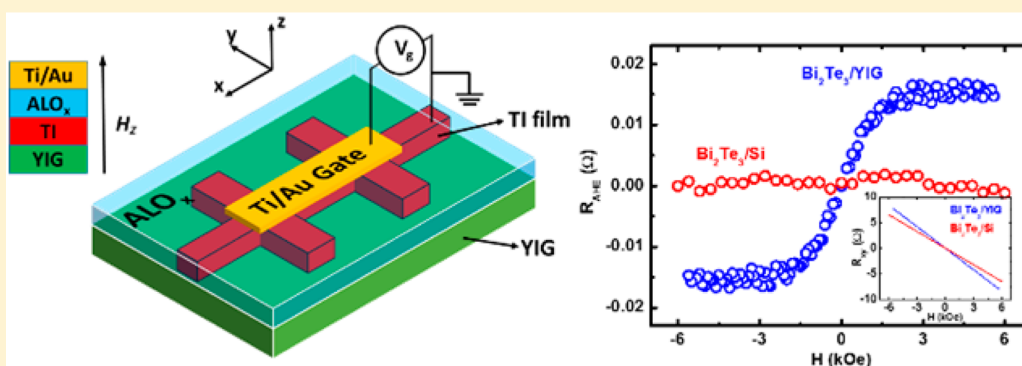

ABSTRACT: The quantum anomalous Hall effect (QAHE) has been recently demonstrated in Cr- and V-doped three-dimensional topological insulators (TIs) at temperatures below 100 mK. In those materials, the spins of unfilled *d*-electrons in the transition metal dopants are exchange coupled to develop a long-range ferromagnetic order, which is essential for realizing QAHE. However, the addition of random dopants does not only introduce excess charge carriers that require readjusting the Bi/Sb ratio, but also unavoidably introduces paramagnetic spins that can adversely affect the chiral edge transport in QAHE. In this work, we show a heterostructure approach to independently tune the electronic and magnetic properties of the topological surface states in $(Bi_xSb_{1-x})_2Te_3$ without resorting to random doping of transition metal elements. In heterostructures consisting of a thin $(Bi_xSb_{1-x})_2Te_3$ TI film and yttrium iron garnet (YIG), a high Curie temperature (~550 K) magnetic insulator, we find that the TI surface in contact with YIG becomes ferromagnetic via proximity coupling which is revealed by the anomalous Hall effect (AHE). The Curie temperature of the magnetized TI surface ranges from 20 to 150 K but is uncorrelated with the Bi fraction x in $(Bi_xSb_{1-x})_2Te_3$. In contrast, as x is varied, the AHE resistivity scales with the longitudinal resistivity. In this approach, we decouple the electronic properties from the induced ferromagnetism in TI. The independent optimization provides a pathway for realizing QAHE at higher temperatures, which is important for novel spintronic device applications.

KEYWORDS: *Topological insulator, magnetic proximity effect, magnetic insulator, anomalous Hall effect, heterostructures, quantum anomalous Hall effect*

Quantum anomalous Hall effect (QAHE) requires both a spontaneous ferromagnetic order and a topological nontrivial inverted band structure.[1−3] To introduce the ferromagnetic order, random doping of transition metal elements, e.g., Cr or V, has been employed.[4−7] Although the Curie temperature (T_C) of the magnetic TI can be as high as ~30 K,[4,7] QAHE only occurs at temperatures 2 orders of magnitude below T_C.[7−10] While the mechanism of this large discrepancy remains elusive, in order to observe QAHE at higher temperatures, it is essential that the exchange interaction in magnetic TI is drastically increased; in the meantime, the magnetic disorder needs to be greatly reduced. For the random doping approach, it is rather difficult to accomplish these two objectives. An alternative way to address both issues simultaneously is to couple a nonmagnetic TI to a high T_C magnetic insulator to induce strong exchange interaction via the proximity effect.[11−13]

The magnetic proximity effect is a well-known phenomenon that has been intensely investigated.[14−20] By proximity coupling, the surface layer of TI acquires a magnetic order without being exposed to any random magnetic impurities.[16−18] This heterostructure approach was previously

Received: May 15, 2015
Revised: August 11, 2015
Published: August 19, 2015

ACS Publications © 2015 American Chemical Society

DOI: 10.1021/acs.nanolett.5b01905
Nano Lett. 2015, 15, 5835−5840

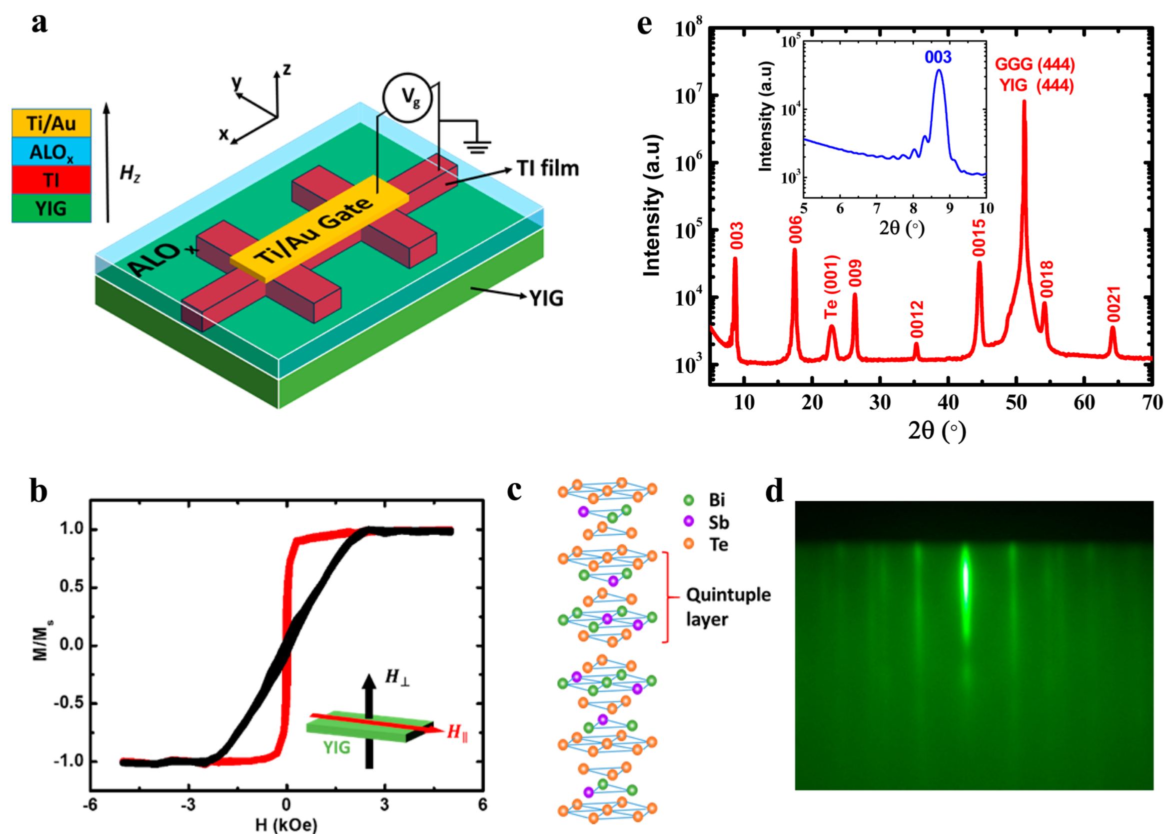

Figure 1. Device schematics and properties of $(Bi_xSb_{1-x})_2Te_3$/YIG thin films. a, Schematic picture of a top-gated 5QL-$(Bi_xSb_{1-x})_2Te_3$/YIG device for magneto-transport measurements with a side view. b, 300 K magnetic hysteresis loops measured by VSM with in-plane and perpendicular magnetic fields. The out-of-plane curve indicates a saturation field ∼2700 Oe which slightly varies in different YIG samples. c, Tetradymite-type crystal structure of $(Bi_xSb_{1-x})_2Te_3$ consisting of quintuple layers. Bi atoms are partially replaced by Sb atoms. d, RHEED pattern of MBE-grown 5 QL-$(Bi_xSb_{1-x})_2Te_3$ on YIG/GGG showing highly ordered flat crystalline surface. e, X-ray diffraction result of a typical 20 QL-$(Bi_xSb_{1-x})_2Te_3$ grown on YIG/GGG. The inset shows a zoom-in view of the (003) peak and clear Kiessig fringes.

adopted in ref 16 using EuS, a ferromagnetic insulator with a band gap of 1.6 eV, and a T_C of ∼16 K, grown on a 20 quintuple-layer (QL) thick Bi_2Se_3. Both magnetoresistance and a small AHE signal at low temperatures were ascribed to an induced magnetization in Bi_2Se_3. Alternatively, YIG has a much larger band gap (∼2.85 eV) and a much higher T_C (∼550 K) and therefore is a better magnetic insulator for heterostructures. In Bi_2Se_3/YIG, the magnetoresistance observed at low temperatures indicates an interaction effect between the two materials.[17,18] We observed suppressed weak antilocalization in 20 QL-Bi_2Se_3 on YIG.[17] Based on our recent successes in Pd/YIG,[20] Bi_2Se_3/YIG,[17] and graphene/YIG,[15] here we demonstrate that high-quality heterostructures of 5 QL thick $(Bi_xSb_{1-x})_2Te_3$ grown on atomically flat YIG films exhibits induced ferromagnetism at the TI surface. By varying the ratio of Bi to Sb, we can effectively tune the electronic properties such as the carrier density and resistance of the TI layer without affecting the magnetic properties of YIG or the induced magnetic layer in TI.

The atomically flat YIG films (∼20 nm) were first epitaxially grown on (111)-gadolinium gallium garnet (GGG) substrates via pulsed laser deposition as described previously.[17,20] Room temperature ferromagnetic resonance (FMR), vibrating sample magnetometry (VSM), and atomic force microscopy (AFM) measurements have been performed on all samples (see Supporting Information). YIG films show clear in-plane magnetic anisotropy (Figure 1b) and the bulk magnetization value ($4\pi M_s$ ∼ 2000 Oe). Then they were transferred to an ultrahigh vacuum molecular beam epitaxy (MBE) system for TI film growth. After high temperature annealing (degassing), 5 QL-thick TI films were grown on YIG and then capped with a 10 nm thick epitaxial Te layer. The sharp and streaky reflection high energy electron diffraction (RHEED) pattern (Figure 1d) of the 5 QL TI indicates a flat surface and well-defined single crystal structure. High single crystal quality was also confirmed by X-ray diffraction (XRD) on a 20 QL TI on (111)-oriented YIG/GGG, as shown in Figure 1e. All peaks can be identified with (00n) diffraction of $(Bi_xSb_{1-x})_2Te_3$, while the YIG/GGG shows the (444) diffraction peak and the (001) peak of the Te capping layer is also present. No other phase is observed in the TI/YIG film according to the XRD data. The zoom-in low-angle XRD scan near the (003)-peak shows multiple Kiessig fringes on both sides, further revealing excellent layered structures of TI films on (111)-oriented YIG and good TI/YIG interface correlation. For transport studies, Hall bars of 900 μm × 100 μm were fabricated by photolithography and etching the TI layers by inductively coupled plasma (ICP). For selected samples, a 50 nm thick Al_2O_3 layer was grown as a top gate dielectric by atomic layer deposition (ALD), and a 80 nm thick Ti/Au layer was deposited by electron beam evaporation to form a top-gated device (Figure 1a).

In this work, we have prepared multiple $(Bi_xSb_{1-x})_2Te_3$ samples with six different Bi fractions, i.e., x = 0, 0.16, 0.24, 0.26, 0.36, and 1. By varying Bi content, the carrier

DOI: 10.1021/acs.nanolett.5b01905
Nano Lett. 2015, 15, 5835−5840

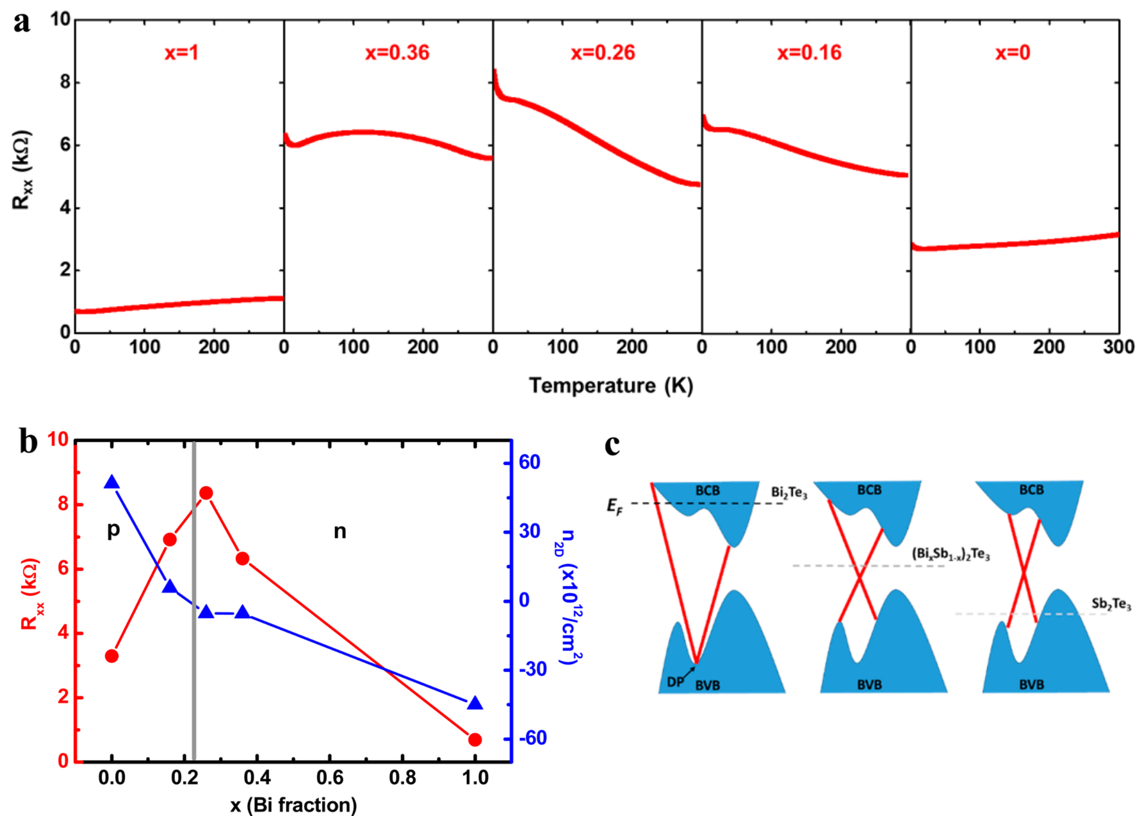

Figure 2. Evolution of the longitudinal resistivity and carrier density with Bi fraction in five 5QL $(Bi_xSb_{1-x})_2Te_3$/YIG films. a, Temperature-dependent longitudinal resistance for five 5QL $(Bi_xSb_{1-x})_2Te_3$/YIG samples with x varying from 0 to 1. b, Longitudinal resistance and carrier density vs Bi fraction. c, Schematic electronic band structure of $(Bi_xSb_{1-x})_2Te_3$ indicating the shift of the Fermi energy as x is varied.

concentrations of TI samples are systematically controlled,[21,22] so that the position of the Fermi level is tuned from the bulk valence band (e.g., $x = 0$), through the band gap (intermediate x's), and to the bulk conduction band (e.g., $x = 1$). The Fermi level position tuning allows us to control the relative contributions to electrical transport from the bulk and surface states. For the surface state-dominated samples (e.g., $x = 0.24$), we can continuously fine-tune the Fermi level across the Dirac point by electrostatic gating.

Figure 2a displays the temperature dependence of five TI/YIG samples. For the Bi_2Te_3 ($x = 1$) and Sb_2Te_3 ($x = 0$) samples at the extreme doping levels, the resistivity (R_{xx}) is lower than that of the other three samples over the entire temperature range. Moreover, these two samples show metallic behaviors, i.e., $dR_{xx}/dT > 0$ over the most temperature range, while the other three samples show a stronger insulating tendency, i.e., $dR_{xx}/dT < 0$, due to depletion of bulk carriers at lower temperatures. Among these three insulating samples, the $x = 0.26$ sample has the highest R_{xx} at 2 K, reaching 8.4 kΩ. Figure 2b summarizes both the 2 K resistivity and the carrier density vs the Bi fraction x. As x increases from 0 to ∼0.16, R_{xx} increases, and the carriers are holes from the Hall measurements. The hole carrier density decreases as x approaches 0.16. The increasing R_{xx}, decreasing 2D carrier density, and the insulating behavior of $x = 0.16$ sample all indicate that the Fermi level shifts up from the bulk valence band into the bulk band gap.[21] As x increases further, the R_{xx} continually increases, and the 2D hole density passes the minimum, and then carriers switch to electrons. These facts suggest that the Fermi level passes the Dirac point of the topological surfaces states between x∼ 0.16 and 0.26. As x increases further, the Fermi level shifts up more and finally enters the bulk conduction band as x approaches 1. Figure 2c illustrates a schematic band diagram when x is varied.[23] The actual band structure and the precise Fermi level position for each x require detailed first-principles calculations. Nevertheless, the relative position of the Fermi level with respect to the Dirac point for different x values can be qualitatively determined from our experimental data.

To probe the proximity-induced ferromagnetism in the TI surface contacting YIG, we focus on the nonlinear Hall signal by removing the dominant linear ordinary Hall background signal.[15,16] The inset of Figure 3a shows a comparison between Bi_2Te_3/YIG and Bi_2Te_3/Si. Both have strong linear Hall signals with negative slopes as expected for an n-type Bi_2Te_3. The carrier density of TI layer is 4.4×10^{13}/cm^2 for Bi_2Te_3/YIG and 5.4×10^{13}/cm^2 for Bi_2Te_3/Si, which is not very sensitive to substrate. However, as the linear background is removed, the remaining Hall signal from the two samples shows a distinct difference. While Bi_2Te_3/Si does not have any definitive nonlinear signal left, Bi_2Te_3/YIG has a clear nonlinear component with a saturation feature. In general, nonlinearity in Hall voltages can arise from coexisting two types of carriers. In fact, such nonlinearity is often observed when the Fermi level is in the vicinity of the Dirac point where both electrons and holes are present.[24] These two samples are clearly in the single carrier type regime; therefore, we exclude the two-carrier possibility. The shape of the nonlinear Hall signal in Bi_2Te_3/YIG resembles that of the YIG hysteresis loop in perpendicular magnetic fields (Figure 1b). We thus assign this nonlinear signal a contribution from AHE. Further evidence will be discussed shortly. Although it is not straightforward to determine the exact physical origin of the observed AHE, it is

DOI: 10.1021/acs.nanolett.5b01905
Nano Lett. 2015, 15, 5835−5840

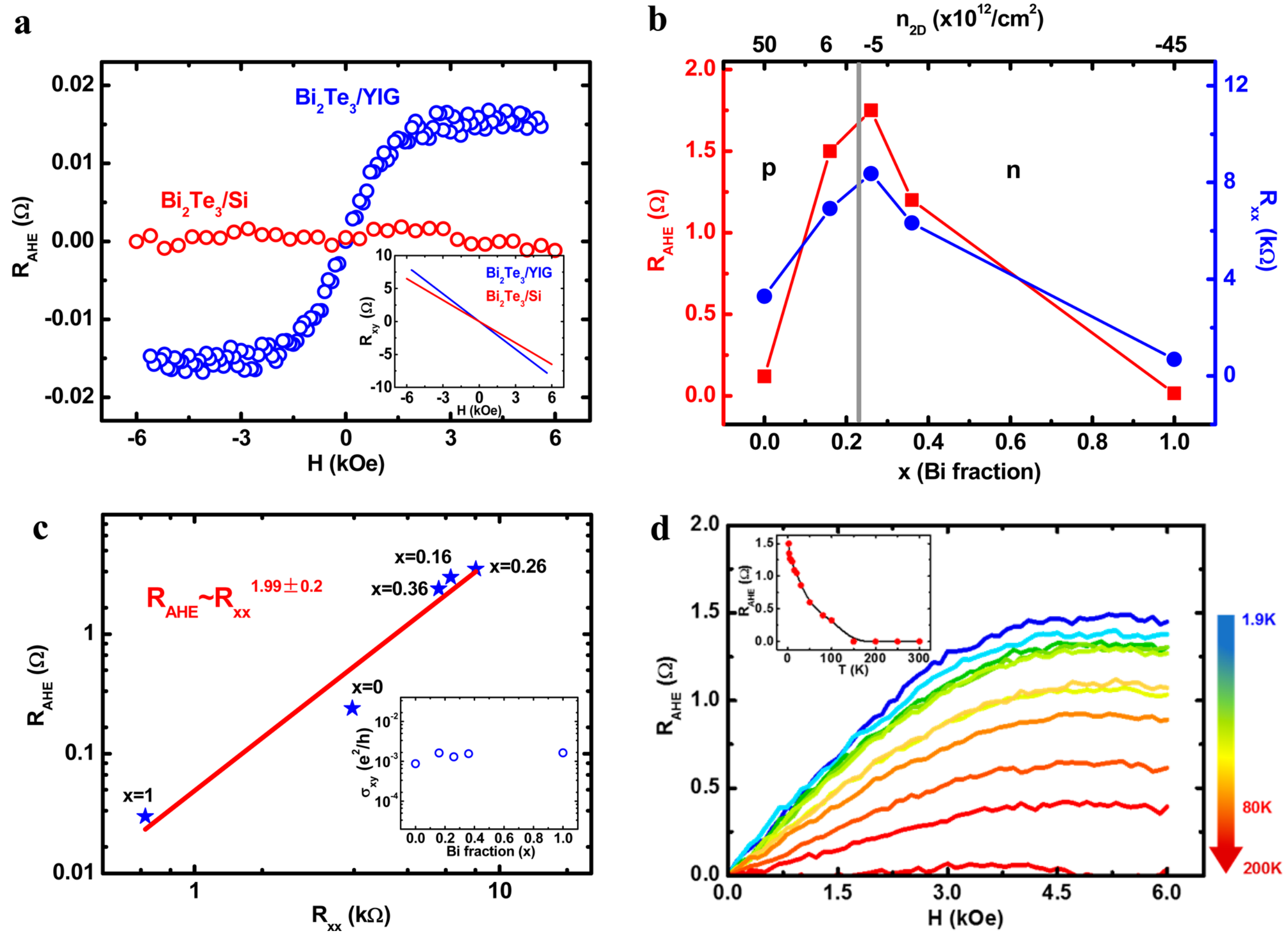

Figure 3. Proximity induced ferromagnetism in $(Bi_xSb_{1-x})_2Te_3$/YIG films. a, A comparison of nonlinear Hall resistivity after the linear Hall background is removed in Bi_2Te_3/YIG and Bi_2Te_3/Si. The inset shows the total Hall data for Bi_2Te_3/YIG and Bi_2Te_3/Si. b, AHE resistance and longitudinal resistance vs Bi fraction (bottom axis) and carrier density (top axis). c, Log–log plot for AHE resistance vs longitudinal resistance for five samples. The slope of the red line is 1.99 ± 0.2. The inset shows σ_{xy}, the AHE conductivity, as the Bi fraction is varied. d, AHE resistance of $(Bi_{0.16}Sb_{0.84})_2Te_3$/YIG sample measured from 2 to 200 K. The inset is the saturated AHE resistance as a function of the temperature showing a T_C of ∼150 K.

known that AHE must stem from ferromagnetism in conductors.[25] Since the underlying YIG is found to remain insulating (resistance >40 GΩ) when measured after the TI growth, etching, and device fabrication are completed, we exclude that the YIG surface itself becomes conducting and contributes to the AHE signal. Moreover, since YIG is grown at ∼700 °C while TI is grown at ∼250 °C later, we do not expect any significant diffusion of Fe atoms to dope the TI to turn it to ferromagnetic. Hence, we conclude that the bottom metallic surface of the TI film becomes ferromagnetic via the proximity coupling just as what has been observed in other systems.[15,16,19,20]

Note that in the Bi_2Te_3 sample (x = 1) the saturation value of the AHE magnitude R_{AHE} is only ∼0.015 Ω, much smaller than R_{xx}. In fact, all samples show clear AHE signals at 2 K. More importantly, as the carrier type switches as x goes from 0.16 to 0.26, the sign of the AHE resistivity remains the same. Since the ordinary Hall effect arises from the Lorentz force associated with an external magnetic field such as the stray magnetic field from domain boundaries, if the nonlinear Hall signal observed here is due to the ordinary Hall effect, its sign would change as the carrier type switches. The absence of the sign change further confirms the AHE nature of the nonlinear Hall signal, i.e., it is a consequence of the induced ferromagnetic surface of TI.[25] Moreover, R_{AHE} follows the same trend as that of R_{xx} (Figure 3b), i.e., the more insulating samples showing larger R_{AHE}. In x = 0.26 sample, R_{AHE} jumps to nearly 2 Ω, over 2 orders of magnitude larger than in Bi_2Te_3 (x = 1). After passing the crossover point, R_{AHE} decreases to 1.5 Ω at x = 0.16 and finally drops to 0.12 Ω at x = 0 (Sb_2Te_3) which is only 10% of the maximum value. Quantitatively, the correlation between R_{xx} and R_{AHE} can be better seen in Figure 3c where a power-law with an exponent ∼2 best fits the data. Since $\rho_{xy} \ll \rho_{xx}$ and $\sigma_{xy} = -((\rho_{xy})/(\rho_{xx}^2 + \rho_{xy}^2))$, this power-law suggests that the AHE conductivity is nearly independent of ρ_{xx}. Since x is the controlling parameter, the quadratic relation between ρ_{xx} and ρ_{xy} suggests that σ_{xy} is constant (shown in the inset of Figure 3c), which rules out the skew scattering mechanism.

The induced ferromagnetism arises from the hybridization between the boundary layers of the two materials in the TI/YIG heterostructures; therefore, the resulting exchange coupling is expected to be weaker than that in the interior of YIG.[16] Additionally, less than ideal interfaces can further weaken the exchange coupling strength. To quantify the exchange interaction of the proximity effect, we measure the AHE signal as the temperature is increased until it vanishes. We define it as the ferromagnetic ordering temperature or T_C for

DOI: 10.1021/acs.nanolett.5b01905
Nano Lett. 2015, 15, 5835−5840

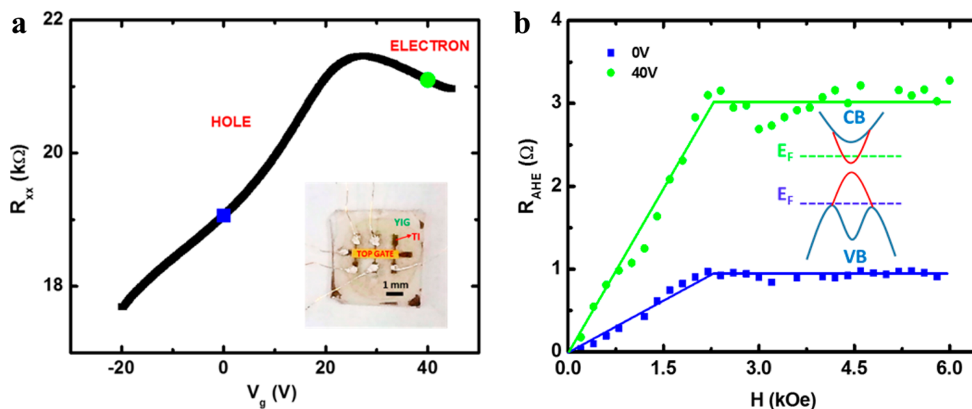

Figure 4. AHE of $(Bi_{0.24}Sb_{0.76})_2Te_3$/YIG films tuned with gate voltage. a, The gate voltage dependence of longitudinal resistance for $x = 0.24$ sample. The blue squares and green circles represent 0 and 40 V top gate voltages, respectively. The inset is the optical image of the top-gated device. b, AHE resistance at different gate voltages with different carrier types: 0 V (hole side) and 40 V (electron side). Solid lines are guides for the eyes. The inset shows a schematic picture of the relative Fermi level position at 0 and 40 V top gate voltages, respectively.

the induced magnetic layer in TI. The T_C of all TI/YIG samples is above 20 K and can be as high as ∼150 K, as shown in Figure 3d. There seems to be no correlation between T_C and x or the carrier concentration (see Figure S5). Instead, this sample-to-sample variation may be attributed to variations in the state of the TI-YIG interface. Although it is not possible to pinpoint the most important factor (e.g., oxidation state and surface termination) responsible for the exchange strength, there is no fundamental reason that the T_C should be limited to 150 K. Future improvement of interface quality is expected to result in a higher T_C of the magnetized layer.

For the insulating samples whose Fermi level is located in the bulk band gap of the TI, we can further fine-tune the position with a gate to access the surface states at different energies. Figure 4a shows the gate voltage dependence of R_{xx} for the $x = 0.24$ sample which has a top gate above a 50 nm thick Al_2O_3 insulator. At zero gate voltage, i.e., $V_g = 0$ V, the temperature dependence shows a bulk insulating behavior and the ordinary Hall data indicates the p-type conduction. Therefore, the Fermi level is located just below the Dirac point in the band gap. As the gate voltage is swept from negative to positive, the resistivity reaches a peak ($R_{xx} \sim 22$ kΩ) at $V_g \sim 25$ V, and the carrier type switches from the p- to n-type as indicated by the ordinary Hall background. As V_g is swept, the Fermi level moves upward and passes the Dirac point which coincides with the maximum in resistivity. The AHE data for two representative gate voltages, i.e., 0 and 40 V, are displayed in Figure 4b. Although the ordinary Hall slope has opposite signs (not shown), the sign of the AHE remains the same on both sides of the Dirac point, which is consistent with the doping dependence discussed earlier. Interestingly, in samples with widely different doping levels, not only is the relative Fermi level position with respect to the Dirac point, but also the band structure is different.[21−23] Here in one sample, the electrostatic gating only shifts the Fermi level in a fixed band structure. Therefore, the fact that the AHE sign remains unchanged across the Dirac point is robust.

Unlike in Cr- or V-doped TI, the ferromagnetism is only induced at the bottom surface of the TI layer in TI/YIG heterostructures. Nevertheless, we have demonstrated an alternative route of introducing stronger exchange interaction to TI surface states by proximity coupling. A stronger exchange should lead to a larger topological gap and, therefore, a higher temperature at which QAHE occurs. In the meantime, by independently optimizing the electronic properties of the TI, we can reduce disorder, especially magnetic disorder, and simultaneously tune the Fermi level position in TI without affecting the induced ferromagnetism.

■ ASSOCIATED CONTENT

Ⓢ Supporting Information

The Supporting Information is available free of charge on the ACS Publications website at DOI: 10.1021/acs.nanolett.5b01905.

Material growth, device fabrication, and additional figures (PDF)

■ AUTHOR INFORMATION

Corresponding Author

*E-mail: jing.shi@ucr.edu.

Notes

The authors declare no competing financial interest.

■ ACKNOWLEDGMENTS

We would like to thank V. Aji for fruitful discussions and W. Beyermann, C.N. Lau, D. Humphrey, R. Zheng, M. Aldosary, and K. Myhro for the technical assistance. Work by Z.L.J. was supported by the UC Lab Fees under Award No. 12-LR-237789. Work by C.T. was supported by NSF ECCS under Award No. 1202559. Work by J.S. was supported by the U.S. Department of Energy (DOE), Office of Science, Basic Energy Sciences (BES) under Award No. DE-FG02-07ER46351. C.Z.C., P.W., and J.S.M. would like to thank support from the STC Center for Integrated Quantum Materials under NSF Grant No. DMR-1231319, NSF DMR Grant No. 1207469, and ONR Grant No. N00014-13-1-0301.

■ REFERENCES

(1) Yu, R.; Zhang, W.; Zhang, H. J.; Zhang, S. C.; Dai, X.; Fang, Z. *Science* **2010**, *329*, 61−64.

(2) Nomura, K.; Nagaosa, N. *Phys. Rev. Lett.* **2011**, *106*, 166802−4.

(3) Liu, C. X.; Qi, X. L.; Dai, X.; Fang, Z.; Zhang, S. C. *Phys. Rev. Lett.* **2008**, *101*, 146802.

(4) Chang, C.-Z.; Zhang, J.; Liu, M.; Zhang, Z.; Feng, X.; Li, K.; Wang, L.-L.; Chen, X.; Dai, X.; Fang, Z.; Qi, X.-L.; Zhang, S.-C.; Wang, Y.; He, K.; Ma, X.-C.; Xue, Q.-K. *Adv. Mater.* **2013**, *25*, 1065−1070.

(5) Kou, X.; Lang, M.; Fan, Y.; Jiang, Y.; Nie, T.; Zhang, J.; Jiang, W.; Wang, Y.; Yao, Y.; He, L.; Wang, K. L. *ACS Nano* **2013**, *7*, 9205−9212.

(6) Kou, X.; He, L.; Lang, M.; Fan, Y.; Wong, K.; Jiang, Y.; Nie, T.; Jiang, W.; Upadhyaya, P.; Xing, Z.; Wang, Y.; Xiu, F.; Schwartz, R. N.; Wang, K. L. *Nano Lett.* **2013**, *13*, 4587−4593.

(7) Chang, C.-Z.; Zhao, W.; Kim, D. Y.; Zhang, H. J.; Assaf, B. A.; Heiman, D.; Zhang, S. C.; Liu, C. X.; Chan, M. H. W.; Moodera, J. S. *Nat. Mater.* **2015**, *14*, 473−477.

(8) Chang, C. Z.; Zhang, J.; Feng, X.; Shen, J.; Zhang, Z.; Guo, M.; Li, K.; Ou, Y.; Wei, P.; Wang, L.; Ji, Z.; Feng, Y.; Ji, S.; Chen, X.; Jia, J.; Dai, X.; Fang, Z.; Zhang, S.; He, K.; Wang, Y.; Lu, L.; Ma, X.; Xue, Q.-K. *Science* **2013**, *340*, 167−170.

(9) Kou, X.; Guo, S.-T.; Fan, Y.; Pan, L.; Lang, M.; Jiang, Y.; Shao, Q.; Nie, T.; Murata, K.; Tang, J.; Wang, Y.; He, L.; Lee, T.-K.; Lee, W.; Wang, K. L. *Phys. Rev. Lett.* **2014**, *113*, 137201.

(10) Checkelsky, J. G.; Yoshimi, R.; Tsukazaki, A.; Takahashi, K. S.; Kozuka, Y.; Falson, J.; Kawasaki, M.; Tokura, Y. *Nat. Phys.* **2014**, *10*, 731−736.

(11) Li, M.; Cui, W.; Yu, J.; Dai, Z.; Wang, Z.; Katmis, F.; Guo, W.; Moodera, J. S. *Phys. Rev. B: Condens. Matter Mater. Phys.* **2015**, *91*, 014427.

(12) Eremeev, S. V.; Men'shov, V. N.; Tugushev, V. V.; Echenique, P. M.; Chulkov, E. V. *Phys. Rev. B: Condens. Matter Mater. Phys.* **2013**, *88*, 144430.

(13) Xu, G.; Wang, J.; Felser, C.; Qi, X. L.; Zhang, S. C. *Nano Lett.* **2015**, *15*, 2019−2023.

(14) Qiao, Z.; Ren, W.; Chen, H.; Bellaiche, L.; Zhang, Z.; MacDonald, A. H.; Niu, Q. *Phys. Rev. Lett.* **2014**, *112*, 116404.

(15) Wang, Z.; Tang, C.; Sachs, R.; Barlas, Y.; Shi, J. *Phys. Rev. Lett.* **2015**, *114*, 016603.

(16) Wei, P.; Katmis, F.; Assaf, B. A.; Steinberg, H.; Jarillo-Herrero, P.; Heiman, D.; Moodera, J. S. *Phys. Rev. Lett.* **2013**, *110*, 186807.

(17) Jiang, Z.; Katmis, F.; Tang, C.; Wei, P.; Moodera, J. S.; Shi, J. *Appl. Phys. Lett.* **2014**, *104*, 222409.

(18) Lang, M.; Montazeri, M.; Onbasli, M.; Kou, X.; Fan, Y.; Upadhyaya, P.; Yao, K.; Liu, F.; Jiang, Y.; Jiang, W.; Wong, K.; Yu, G.; Tang, J.; Nie, T.; He, L.; Schwartz, R.; Wang, Y.; Ross, C.; Wang, K. L. *Nano Lett.* **2014**, *14*, 3459−3465.

(19) Huang, S. Y.; Fan, X.; Qu, D.; Chen, Y. P.; Wang, W.; Wu, J.; Chen, T.; Xiao, J.; Chien, C. L. *Phys. Rev. Lett.* **2012**, *109*, 107204.

(20) Lin, T.; Tang, C.; Shi, J. *Appl. Phys. Lett.* **2013**, *103*, 132407.

(21) Zhang, J.; Chang, C. Z.; Zhang, Z.; Wen, J.; Feng, X.; Li, K.; Liu, M.; He, K.; Wang, L.; Chen, X.; Xue, Q.; Ma, X.; Wang, Y. *Nat. Commun.* **2011**, *2*, 574.

(22) Kong, D.; Chen, Y.; Cha, J. J.; Zhang, Q.; Analytis, J. G.; Lai, K.; Liu, Z.; Hong, S. S.; Koski, K. J.; Mo, S.-K.; Hussain, Z.; Fisher, I. R.; Shen, Z.-X.; Cui, Y. *Nat. Nanotechnol.* **2011**, *6*, 705−709.

(23) Zhang, H.; Liu, C.-X.; Qi, X.-L.; Dai, X.; Fang, Z.; Zhang, S.-C. *Nat. Phys.* **2009**, *5*, 438−442.

(24) Bansal, N.; Kim, Y.; Brahlek, M.; Edrey, E.; Oh, S. *Phys. Rev. Lett.* **2012**, *109*, 116804.

(25) Nagaosa, N.; Sinova, J.; Onoda, S.; MacDonald, A. H.; Ong, N. P. *Rev. Mod. Phys.* **2010**, *82*, 1539−1592.

DOI: 10.1021/acs.nanolett.5b01905
Nano Lett. 2015, 15, 5835−5840